JACS
JOURNAL OF THE AMERICAN CHEMICAL SOCIETY
pubs.acs.org/JACS
Article

Irreversible Lattice Expansion Effects in Nanoscale Indium Oxide for CO_2 Hydrogenation Catalysis

Chenyue Qiu,[▽] Junchuan Sun,[▽] Mengsha Li,[▽] Chengliang Mao, Rui Song, Zeshu Zhang, Doug D. Perovic, Jane Y. Howe,* Lu Wang,* and Geoffrey A. Ozin*

Cite This: https://doi.org/10.1021/jacs.4c12985

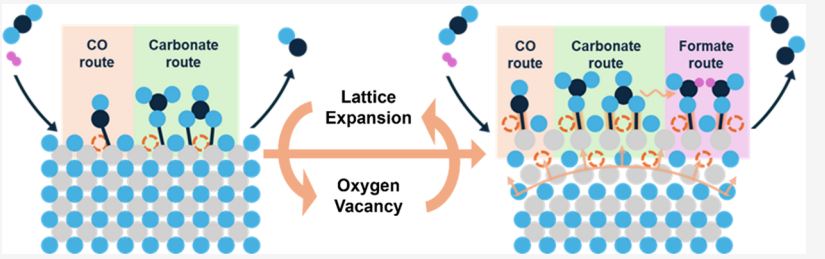

ABSTRACT: Thermal energy has been considered the exclusive driving force in thermochemical catalysis, yet associated lattice expansion effects have been overlooked. To shed new light on this issue, variable temperature *in situ* high-resolution (scanning) transmission electron microscopy (HR-(S)TEM) and electron energy-loss spectroscopy (EELS) were employed to provide detailed information on the structural changes of an archetype nanoscale indium oxide materials and how these effects are manifest in reverse water gas shift heterogeneous catalytic reactivity. It is found that with increasing temperature and vacuum conditions, an irreversible surface lattice expansion is traced to the formation and migration of oxygen vacancies. Together, these changes are believed to be responsible for the decreased activation energy and improved reaction rate observed for the reverse water gas shift reaction. Studies of this kind provide new insight into how thermal energy affects thermochemical heterogeneous catalysis.

1. INTRODUCTION

It has long been known that in the field of physical science, expansion of matter can be achieved by heat treatment.[1] A specific constant describes the degree of the expansion of solid-state materials, namely, the coefficient of expansion.[1] Based on the thermally enhanced vibrations and induced displacement of the constituent atoms, the heated substance usually expands volumetrically. This rule has functioned well for centuries with respect to bulk materials but is more of a challenge for nanomaterials.[2,3]

Heterogeneous catalysis, involving the interaction of a gaseous reactant with the surface of a solid to form a product, is dominated by thermocatalysis, a process which is responsible for producing commodity chemicals and fuels for society.[4−9] In a thermally enabled heterogeneous catalytic process, thermal energy is typically considered as the sole driving force, and the effect of temperature on changes in the structure−property relations of the catalyst has essentially been forgotten.[8,10,11] Since thermally driven reactions occur at surface-active sites of a heterogeneous catalyst, it is expected that a thermally created defect and corresponding expanded surface must somehow influence surface chemical reactions and overall catalytic performance.

With the emergence of *in situ* high-resolution surface characterization techniques, detailed information can be obtained on the surface structure of heterogeneous catalysts under a wide range of operating conditions.[12−15] Herein, an archetype indium oxide reverse water gas shift heterogeneous catalyst is studied by variable temperature *in situ* (scanning) transmission electron microscopy ((S)TEM), electron energy-loss spectroscopy (EELS), X-ray diffraction (XRD), X-ray photoelectron spectroscopy (XPS), and diffuse reflectance infrared Fourier transform spectroscopy (DRIFTS). Information obtained from these analytical techniques unveils the strong correlation between thermally induced oxygen vacancy formation and lattice expansion on the rates of the reverse water gas shift reaction. These experimental findings are further substantiated by density functional theory (DFT) simulations, which provide structural information about the effect of temperature on the surface and bulk domains of indium oxide nanocrystals.

Received: September 18, 2024
Revised: November 21, 2024
Accepted: November 21, 2024

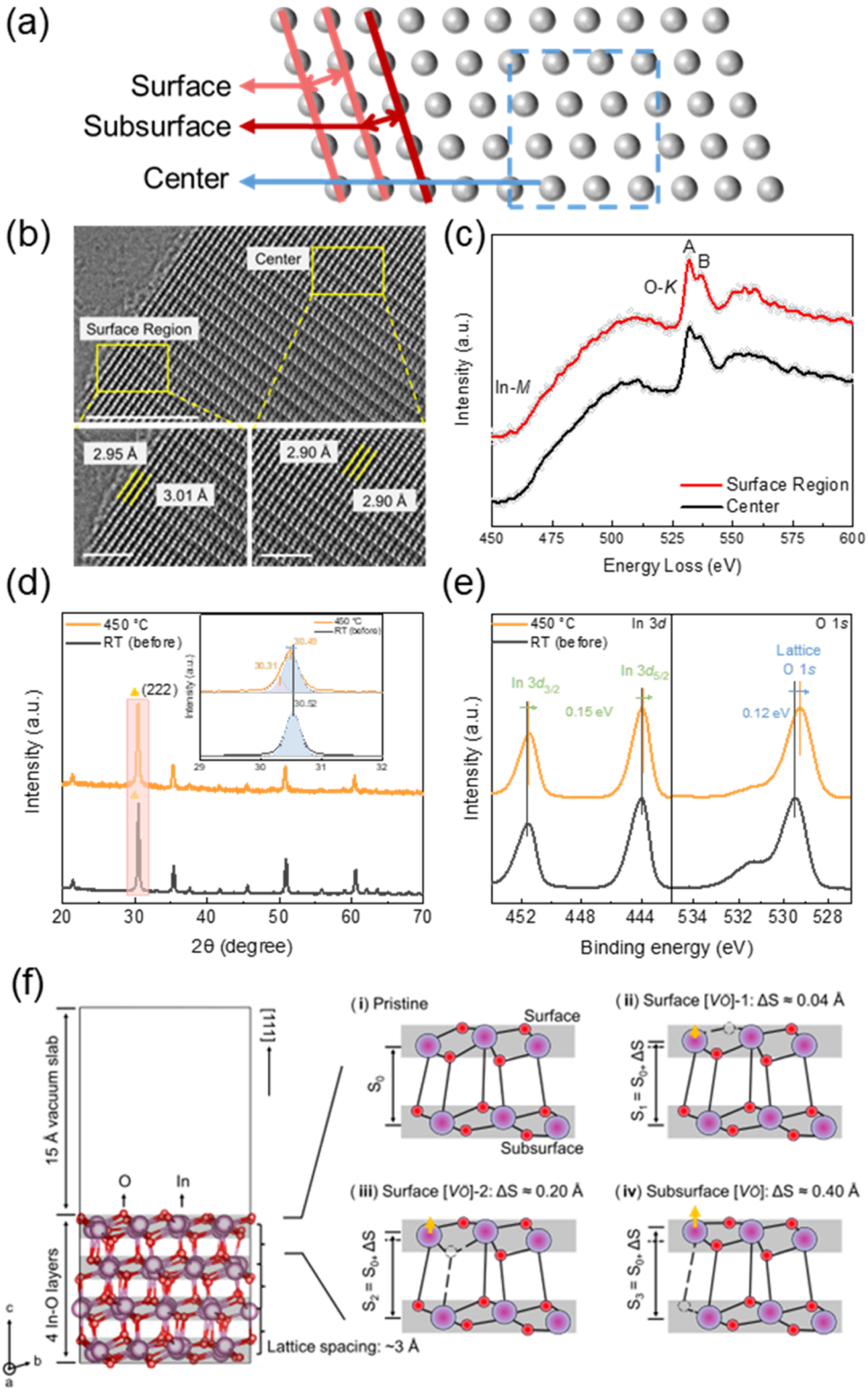

Figure 1. Structural Analysis. (a) Schematic diagram of lattice matrix defined as surface, subsurface, and center (bulk). (b) Aberration-corrected TEM image of In_2O_3 NP annealed at 450 °C under vacuum. Scale bar: 5 nm. The enlarged images are extracted from the regions labeled by yellow rectangles in the corresponding HRTEM images. Scale bar: 2 nm. (c) EEL spectra of In-*M* edge and O-*K* edge collected from the surface and center regions of the vacuum calcined In_2O_3 NP in panel (b). The dots are experimental data, and the solid lines are smoothed data using the fast Fourier Transform only for guiding the eye. (d) *In situ* XRD patterns of In_2O_3 (222) planes annealed from RT to 450 °C under vacuum. (e) *In situ* XPS In 3*d* and O 1*s* spectrum of In_2O_3 annealed from RT to 450 °C under vacuum. (f) DFT geometry optimization of (111) facet-exposed In_2O_3 model and corresponding simplified ball−stick models for (i) pristine sample and oxygen vacancy (dashed circle) on (ii) surface lower site, (iii) upper site, and (iv) subsurface. S_0 in model i represents the pristine lattice spacing between surface and subsurface In−O layers, while ΔS with their values labeled in models ii, iii, and iv are the lattice expansion induced by the displacement (indicated by the orange arrow) of the surface In atom vicinal to the oxygen vacancy.

https://doi.org/10.1021/jacs.4c12985
J. Am. Chem. Soc. XXXX, XXX, XXX−XXX

2. RESULTS AND DISCUSSION

Aberration-corrected high-resolution TEM (HRTEM) imaging is used to examine the structural changes of In_2O_3 nanoparticles (NPs) calcined at 450 °C under vacuum in a tubular furnace (defined as "vacuum calcined" In_2O_3). To enhance clarity in comprehending the various forms of In_2O_3 mentioned in this work, Table S1 was prepared. As demonstrated in Figure 1a, the outermost lattice is defined as the surface, and the second outermost lattice is defined as "subsurface." As shown in Figure S1a,b, the pristine In_2O_3 NP, synthesized based on a previous report,[16] has the cubic bixbyite structure ($Ia\bar{3}$) with a standard (222) lattice plane *d*-spacing of 2.91 Å at both surface and center regions at room temperature (RT: 24 °C). As for vacuum calcined In_2O_3 NPs, it was observed that the d_{222}-spacing expanded by 6.8% to 3.11 Å for both surface and subsurface lattice planes, whereas the d_{222}-spacing of the center (bulk) regions remained at 2.91 Å (Figure 1b). It is notable that the theoretical thermal expansion value for the (222) plane is ∼0.007 Å (i.e., the coefficient of thermal expansion is 6.2×10^{-6} $°C^{-1}$), which is negligible compared to the lattice expansion measured in this work (Table S2).[17] To further investigate the mechanism of the observed surface lattice expansion, STEM-EELS was used. Figures S1c and 1c present energy-loss near-edge structures (ELNES) of the O-*K* and In-*M* edges acquired from the surface and center regions of the pristine and vacuum calcined In_2O_3 NPs, respectively. Since the In-*M* edge (M_5: 443 eV) is difficult to be deconvoluted from the O-*K* edge, and the indium ion is maintained at a valence state of 3^+ (Figure S2c), we focused on characterizing the O-*K* edge. The two peaks (Peak A: 532 eV, Peak B: ∼537 eV) are ascribed to the hybridization of O 2*p* and In 5*s* and In 5*p* states.[18] Since the peak intensity is sensitive to the electronic structure, the intensity ratio between Peak A and Peak B is a strong indicator of oxygen vacancy concentration ([Vö]) due to the formation of a deep donor state.[19] In the case of pristine In_2O_3, the intensity ratios are calculated as 1.05 ± 0.01 and 1.046 ± 0.02 at the surface and center regions, respectively, which are similar to the standard value extracted from stoichiometric In_2O_3.[20] By comparison, for vacuum calcined In_2O_3, the intensity ratios decrease to 0.849 ± 0.01 and 0.889 ± 0.008 at the surface and center regions, respectively. Accordingly, it was determined that more Vö are generated at the surface rather than the center region.[21]

Moreover, *in situ* XRD and *ex situ*/*in situ* XPS were performed to explore the structural changes of In_2O_3 NPs. Figure 1d presents the *in situ* XRD results of In_2O_3 NPs annealed from RT to 450 °C under a vacuum. Figure 1d (inset) shows the peaks of the (222) plane at RT and 450 °C. The peak located at 30.52° corresponds to a *d*-spacing of 2.92 Å, which is the standard *d*-spacing of the (222) lattice plane at RT. As the temperature increased from RT to 450 °C, a small peak appeared at the diffraction angle of 30.31°, which corresponds to a *d*-spacing of 2.95 Å. Such an enlarged *d*-spacing value indicates the presence of thermally induced lattice expansion.[22] Since the TEM results demonstrate that the lattice expansion mainly occurs in the near-surface region, *in*/*ex situ* XPS were used to analyze the surface changes of In_2O_3 NPs. Figures 1e and S3 show the *in situ* XPS results of In_2O_3 NPs annealed from RT to 450 °C under a vacuum. Interestingly, slight negative energy shifts (lower binding energy) were observed for both In 3*d* and O 1*s* peaks as the temperature was increased from RT to 450 °C. For In 3*d* core level, the decrease in binding energy may be related to lattice expansion[23] and/or the formation of oxygen vacancies (Vö).[24,25] To be specific, lattice expansion results in a larger interatomic distance to make a "looser" structure, thereby reducing the interaction between atoms and leading to a decrease in binding energy.[23,26,27] For the formation of Vö, the O^{2-} ligands will transfer more of their lone pair electron density to In^{3+} in the coordinately unsaturated InO_x, resulting in a lower binding energy. On the contrary, for O 1*s* core level, a positive energy shift will occur owing to the electron transfer to In^{3+}, causing a decrease in charge density of O^{2-} when Vö are formed.[25,28] Therefore, such negative energy shifts of In 3d and O 1s could be speculated to be dominated by lattice expansion, and similar decreasing binding energy trends were also confirmed by the *ex situ* XPS results of pristine and vacuum calcined samples (Figure S2). In order to further confirm the credibility of the above binding energy changes, we also performed higher-resolution synchrotron radiation XPS (SR-XPS) tests and reconfirmed similar shifts (Figure S4). On the other hand, the changes in near-surface region Vö could be detected by XPS as well. Typically, the peak at ∼529.5 eV originates from lattice O in the matrix of metal oxide. The generation of shoulder peak at higher binding energy (∼531.2 eV) could be attributed to various factors,[29] and most reports indicate that it is related to Vö in In_2O_3 systems.[30,31] Thus, we tend to assign the ∼531.2 eV peak to the O-containing species adsorbed on the surface Vö to reflect the intensity of the Vö.[32−35] It is hard to get real information about surface Vö due to the escape of surface-adsorbed species during the vacuum heating process in *in situ* XPS testing (Figure 1e). Fortunately, *ex situ* XPS results can evidence that the surface Vö concentration increases from 34.21 to 36.31% after the vacuum calcination treatment process (Figure S2d and Table S3). In addition, the color change and the red shift of the absorption band in the optical spectrum of pristine and vacuum calcined samples also confirm the increasing concentration of *Vö* after the vacuum calcination process (Figure S5).[36] The above results reveal the existence of lattice expansion and Vö formation at the surface region of In_2O_3 NPs during the vacuum calcination treatment. However, the correlation between lattice expansion and Vö formation is still yet to be understood.

In this regard, spin-polarized density functional theory (DFT) simulations were performed to provide mechanistic insight into the *Vö* formation-induced geometric alteration. The calculation is based on a (111)-facet-exposed cubic In_2O_3 model consisting of four In−O layers (Figures 1f and S6). The distance between the surface and subsurface In−O layers in the DFT model represents the lattice *d*-spacing observed in HRTEM imaging. Thus, the correlation between lattice expansion and Vö formation can be investigated by checking the distance between surface and subsurface In−O layers with and without Vö, specifically, the displacement of In atoms along the [111] direction. While metal cations in a lattice tend to relax to reach a free energy minimum when a vicinal defect or vacancy is formed, the displacement of In is expected by the introduction of a vicinal Vö.[37] Guided by this idea, two types of octahedral O atoms at upper and lower positions within an In−O layer were identified by a lattice analysis. Therefore, there are at least three types of Vö contributing to the surface lattice expansion: the upper surface Vö (Vö-1), the lower surface Vö (Vö-2), and the subsurface Vö (Figure 1f ii−iv).

https://doi.org/10.1021/jacs.4c12985
J. Am. Chem. Soc. XXXX, XXX, XXX−XXX

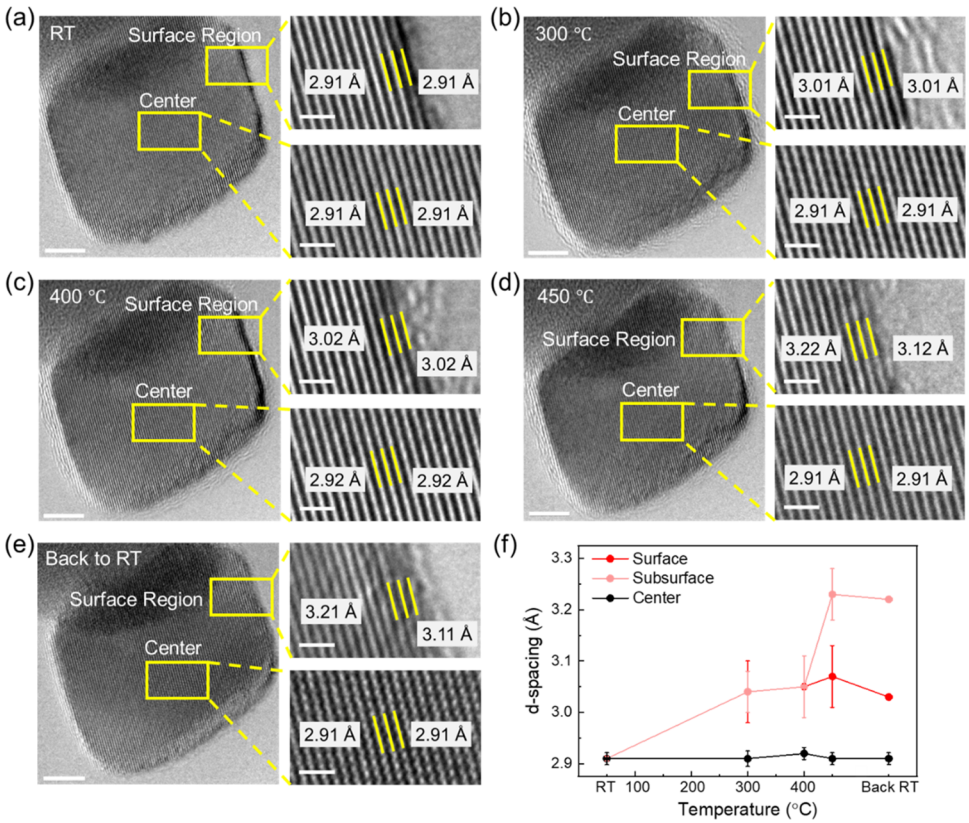

Figure 2. ***In Situ*** HRTEM Structural Analysis. (a−e) HRTEM images of In_2O_3 NP at RT, 300, 400, 450 °C, and back to RT, respectively. Scale bar: 5 nm. The enlarged images are extracted from the regions labeled by yellow rectangles in the corresponding HRTEM images. Scale bar: 1 nm. (f) Summarized trend of In_2O_3 d_{222}-spacing changes at various temperatures at the surface, subsurface, and center regions.

Geometry optimization suggested that respective In displacements were 0.04, 0.20, and 0.40 Å along the [111] direction after the introduction of Vö-1, Vö-2, and subsurface Vö into the In_2O_3 lattice (Figure S7). This suggested the lattice expansion is a consequence of the movement of surface Vö-vicinal In atom toward the vacuum slab and that the Vö at the subsurface can induce the largest lattice expansion among all three possible sites. Furthermore, given Vö is typically dynamic within an oxide lattice, the result also implied that an increased lattice expansion would be expected, if Vö could migrate from surface to subsurface.[38] To check the feasibility of Vö formation on the surface via In_2O_3 + vacuum = In_2O_{3-x} + x/$2O_2$ and Vö migration from the surface to subsurface in the In_2O_{3-x} lattice, a free energy diagram of these processes was computed. The result suggested that Vö formation at 1% concentration should overcome energy barriers of 0.54 eV (Vö-1) and 1.01 eV (Vö-2), respectively (Figure S8). Interestingly, the migration of 1% Vö-1 and Vö-2 to subsurface Vö was slightly "up-hill" (0.14 eV) and "down-hill" (−0.33 eV), respectively, suggesting the migration of Vö-2 to subsurface is spontaneous upon formation. On the other hand, doubling the concentration of [Vö-1] and [Vö-2] to 2% should overcome much higher energy barriers of 2.09 and 2.17 eV, respectively. If these energies are met by thermal heating, the formed [Vö] will spontaneously migrate from the surface to the subsurface. These results suggested high temperatures are needed to enrich Vö-1 and Vö-2 on the In_2O_3 surface, while their migration to the subsurface is spontaneous once the input is larger than 0.68 eV. Following the Vö migration from surface to subsurface, lattice expansion of In_2O_3 will increase.

To understand the relationship between Vö formation and lattice expansion during the vacuum calcination process, *in situ* heating TEM was conducted under vacuum (~10^{-4} Pa) to reveal the dynamic structure evolution of Vö formation and correlated surface lattice expansion at high resolution. As shown in Figure S9, the particle size of the In_2O_3 NPs is measured as 32 ± 6 nm at RT. During the heating process, NPs retained the original particle shape and size (Figure S10), and no phase transformation was observed (Figure S11).

Each set of HRTEM images in Figure 2 focused on the same nanoparticle with overviews and lattice fringes in the surface and center regions. As shown in Figure 2a−e, the exposed facet is the (222) plane with measured *d*-spacings of 2.91 Å at both surface and center regions under RT, which matches the XRD results in Figure S1a. When the temperature increased to 300 °C, the surface and subsurface lattices expanded from 2.91 to 3.01 Å (3.4%), which is maintained at 400 °C. The expansion value measured at these temperatures is significantly larger than that of theoretical thermal expansion (Table S2). When the temperature increased to 450 °C, the surface and subsurface lattices expanded from 2.91 to 3.12 Å (6.8%) and 3.22 Å (10.7%), respectively. However, it is noticeable that no obvious expansion was measured at the center region. Interestingly, when the temperature decreased to RT, the expanded surface and subsurface *d*-spacings were still maintained as 3.11 and 3.21 Å, respectively. Meanwhile, the *d*-spacing of the center region remained at 2.91 Å. The intensity profiles applied to extract the d_{222}-spacings of In_2O_3 at different temperatures are shown in Figure S12, and the results are summarized in Figure 2f. The error bars were generated

https://doi.org/10.1021/jacs.4c12985
J. Am. Chem. Soc. XXXX, XXX, XXX−XXX

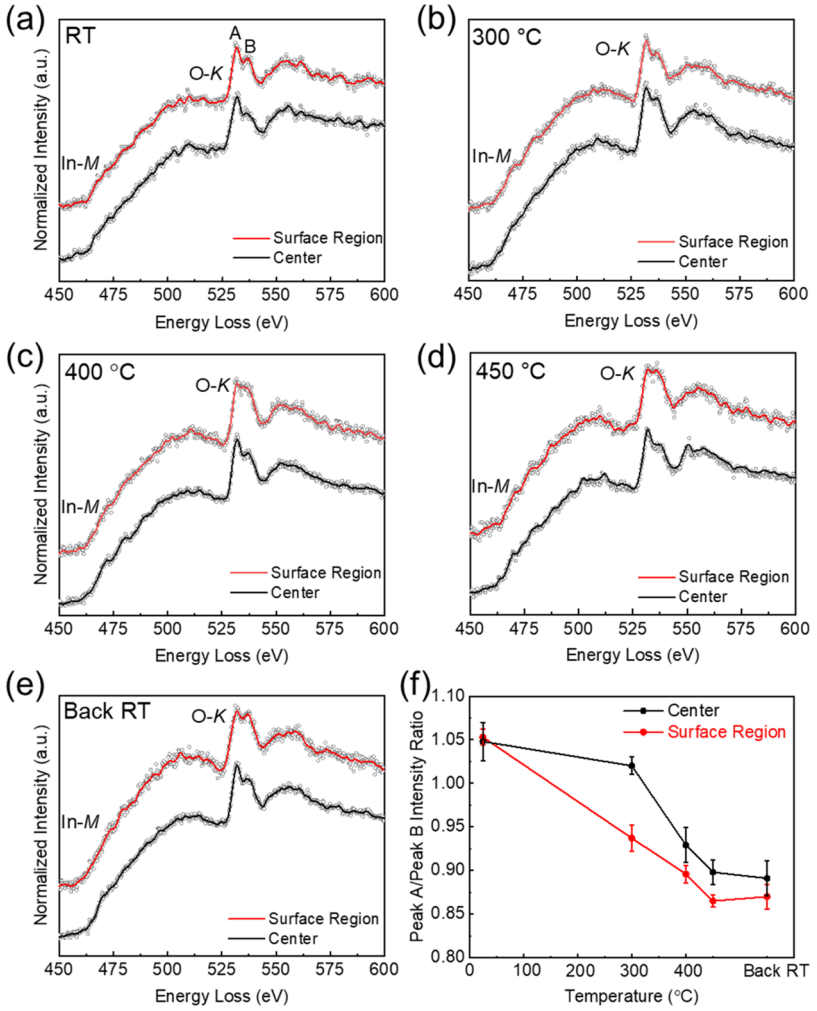

Figure 3. ***In Situ*** STEM-EELS of Vö **Analysis**. (a−e) EEL spectra of In-*M* edge and O-*K* edge at the surface region of In_2O_3 NPs collected from different temperatures: RT, 300, 400, 450 °C, and back to RT, respectively. (f) Peak A/Peak B intensity ratio extracted from the O-*K* edge at the surface In_2O_3 at various temperatures. For each spectrum, the dots are experimental data, and the solid lines are smoothed data using fast Fourier Transform.

based on the measurements from five different particles and several sets of experiments. The *in situ* HRTEM imaging findings agree with the *ex situ* HRTEM and DFT results in Figure 1 in that the Vö formation induces the surface lattice expansion, well beyond the theoretical thermal expansion (Table S2). In our work, electron-beam-induced effects were evaluated and excluded (Figures S13−S15). The irreversible changes of the expanded surface and subsurface *d*-spacings caused by heating are novel compared with the traditional thermal expansion effect. Accordingly, the oxygen vacancies accommodating lattice expansion are of the nonequilibrium (irreversible) vacancy type.

To understand the irreversible expansion of the surface and subsurface *d*-spacings and the correlations to Vö formation, *in situ* STEM-EELS analyses were conducted to investigate surface chemistry or bonding signatures during the heating and cooling process. Figure 3a−e shows the ELNES of the O-*K* and In-*M* edges acquired from the surface and center regions of the In_2O_3 NPs at RT, 300, 400, and 450 °C and back to RT, respectively. The intensity ratios between Peak A and Peak B at RT are calculated as 1.053 ± 0.009 and 1.048 ± 0.02 at the surface and center regions, respectively, similar to the standard value extracted from the *ex situ* pristine In_2O_3 (Figure S1) and stoichiometric In_2O_3.[20] As shown in Figure 3b, at 300 °C, the intensity ratios are 0.937 ± 0.002 and 1.02 ± 0.01 at the surface and center regions, respectively, slightly decreasing but still similar to those at RT. As the temperature increases to 450 °C (Figure 3d), the intensity ratios at the surface and center regions drop to 0.865 ± 0.007 and 0.898 ± 0.014, respectively, which are maintained when the temperature cools back to RT (Figure 3e). Figure 3f summarizes the Peak A/Peak B intensity ratio trend at various temperatures, and exact intensity ratios are presented in Table S4. The decreasing intensity ratio initiates at 300 °C, indicating the increasing [Vö] remains unchanged when the temperature cools back to RT.[21] It also reveals that more Vö is generated at the surface rather than in the center region. These *in situ* results are consistent with *ex situ* EELS characterization (Figure 1c) and confirm the existence of surface Vö formation, which is most likely related to surface lattice expansion. Based on the *in situ* HRTEM and EELS analysis, the temperatures of the irreversible Vö formation agree with those of the surface lattice expansion, matching the results obtained from DFT calculations that surface lattice expansion is attributed to surface Vö formation.

To further understand the relationship between the Vö-lattice expansion and catalytic performance, it is essential to

https://doi.org/10.1021/jacs.4c12985
J. Am. Chem. Soc. XXXX, XXX, XXX−XXX

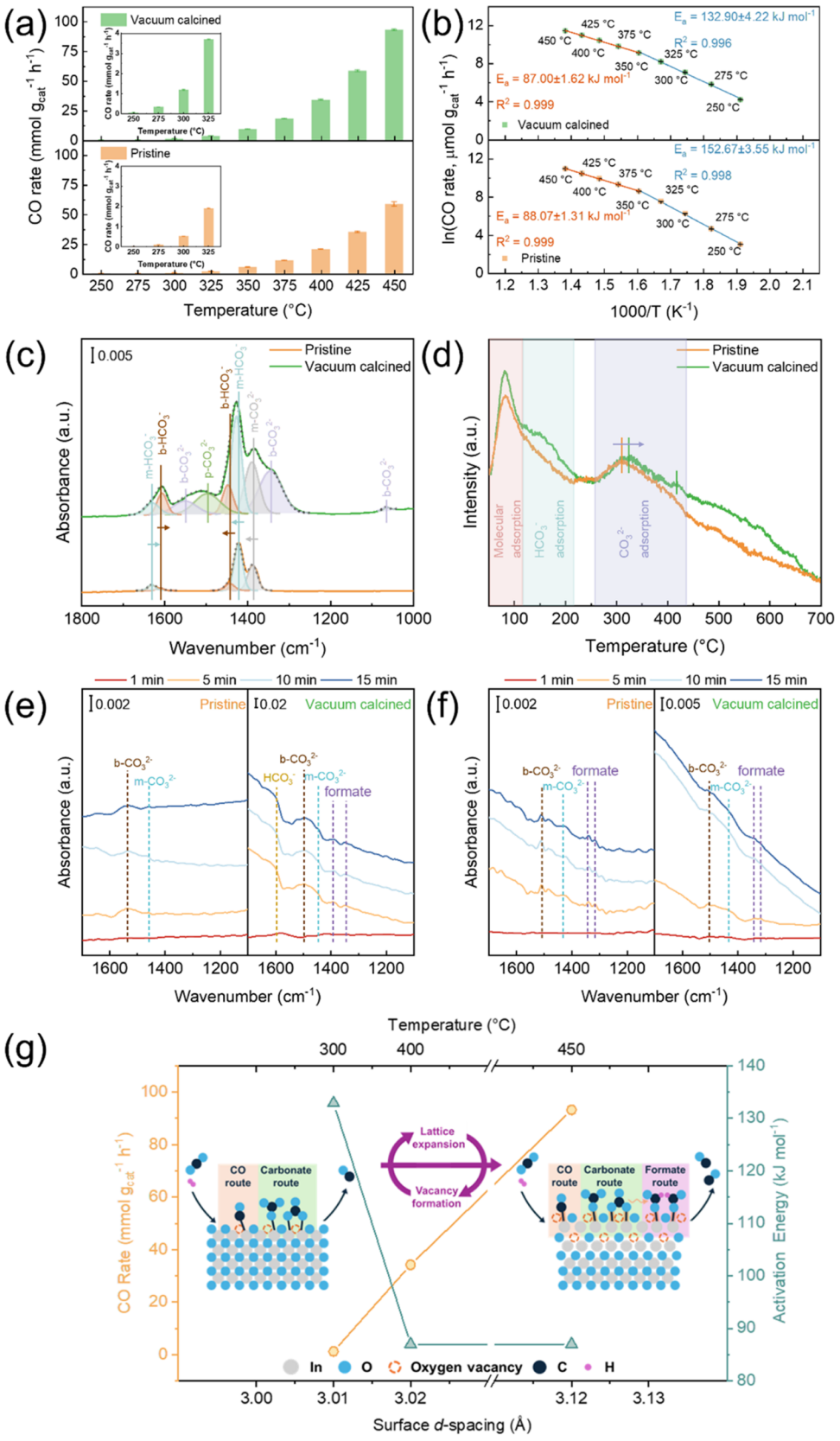

Figure 4. Catalytic Performance and Mechanism Exploration. (a) CO rate of pristine and vacuum calcined samples at different temperatures. Conditions: H_2/CO_2 ratio = 1:1 with a flow rate of 12 mL min^{-1}. (b) Activation energy measurement of RWGS reaction of pristine and vacuum calcined samples. (c) *In situ* DRIFTS spectra of CO_2 adsorption of pristine and vacuum calcined samples at room temperature. Conditions: CO_2/He ratio = 1:9 with a flow rate of 20 mL min^{-1}. (d) CO_2-TPD profiles of pristine and vacuum calcined samples. (e, f) *In situ* DRIFTS spectra of pristine and vacuum calcined samples at (e) 250 and (f) 450 °C. Conditions: H_2/CO_2/He ratio = 1:1:8 with a flow rate of 20 mL min^{-1}. (g) Schematic diagram of the proposed mechanism on lattice expansion effects promoting CO_2 hydrogenation over the In_2O_3 surface.

https://doi.org/10.1021/jacs.4c12985
J. Am. Chem. Soc. XXXX, XXX, XXX−XXX

evaluate the thermally driven catalysis, such as CO_2 hydrogenation.[39] The In_2O_3 NPs were chosen as the archetype model for the RWGS catalytic reaction study. The vacuum thermally treated sample exhibits superior CO activity at each temperature compared to that of the pristine sample (Figure 4a). The increment in the catalytic activity of the vacuum calcined sample over that of the pristine sample decreases versus temperature increasing with the inflection point at 350 °C (Figure S16), which is similar to the apparent activation energy (E_a) trend discussed below. Interestingly, the corresponding Arrhenius plots of both samples present similar two-stage convex plots with the inflection point at 350 °C (Figure 4b), indicating that the increasing temperature may overcome a specific energy barrier and enable a new reaction pathway for RWGS.[40] At lower temperatures (<350 °C), the apparent activation energy of the vacuum calcined sample is 14.88% lower than that of the pristine sample. With increasing temperatures (>350 °C), both samples exhibit similar activation energies (87−88 kJ/mol). Such results indicate that the remaining irreversible lattice expansion and/or Vö formation on the vacuum calcined sample may reduce the E_a to result in an obvious activity increment at lower temperatures.[41] However, with an increase in temperature, the pristine sample eventually exhibits lattice expansion with an increasing amount of Vö, and the difference between both samples becomes inconspicuous.

The CO_2 adsorption/desorption behaviors of pristine and vacuum calcined samples were studied to distinguish the role of lattice expansion and/or Vö formation. Figure 4c represents the *in situ* DRIFTS of the CO_2 adsorption of both samples at room temperature. Since Vö is the recognized active site for CO_2 adsorption, the adsorption capacity of CO_2 is generally positively correlated with the amount of Vö.[25,42,43] After exposure to CO_2, the overall higher CO_2 adsorption intensity of the vacuum calcined sample demonstrates a richer Vö on its surface than that on the pristine sample (Figure 4c), which is consistent with the Vö results we mentioned before. In addition, there are also some differences in the adsorbed species of the two samples. For the pristine sample, only slight mono- and bidentate bicarbonate (m-/b-HCO_3^-)[44,45] and monodentate carbonate (m-CO_3^{2-})[16,44,46] are detected due to the little surface-adsorbed water and rare surface Vö. On the contrary, besides the species mentioned above, we could also find higher coordination CO_2 adsorbed species, including bidentate carbonate (b-CO_3^{2-})[16,46,47] and polydentate carbonate (p-CO_3^{2-}).[48,49] Such results indicate that more surface Vö could promote CO_2 strongly binding to the catalyst surface via higher coordination species, which may be conducive to further hydrogenation.[49] Notably, the 5−10 cm^{-1} red shifts of ν_{as}(OCO) (>1500 cm^{-1}) of m-/b-HCO_3^- (opposite shifts of their ν_s(OCO) (<1500 cm^{-1})) are found between the vacuum calcined sample and the pristine sample, which reveals that the adsorption strength of CO_2 on the vacuum calcined sample is stronger than that on the pristine sample.[50−52] This is speculated to be due to the decrease in binding energy caused by lattice expansion, allowing more electrons to be delivered to the antibond orbital of CO_2.[52] Moreover, the CO_2 desorption studies on CO_2-temperature-programmed desorption (TPD) profiles show similar results (Figure 4d). The overall higher intensity of the vacuum calcined sample also indicates a positive dependence of CO_2 adsorption on surface Vö concentration.[53] The delay of the desorption peak to the high temperature (∼10 °C) and the emergence of new desorption peaks in the CO_3^{2-}-related region illustrate the improvement of adsorption strength and the increase of adsorption species as well.[49,54]

Subsequently, *in situ* DRIFTS was also conducted to track the surface-adsorbed species in order to study the difference in the mechanism at 250 °C (Figures 4e and S17) and 450 °C (Figures 4f and S18) of the pristine and vacuum calcined samples. As shown in Figure 4e−f, the vacuum calcined sample exhibits stronger signals of all species than the pristine sample when the reaction equilibrium is reached, which is owing to the more Vö active sites, as we mentioned above. These results agree well with the catalytic performance trends (Figure 4a). To be specific, the peaks at 2077 and 2055 cm^{-1} can be assigned to diagnostic vibrational modes of adsorbed *CO species, which leads to a direct CO_2 dissociation pathway for CO synthesis (Figure S17).[55,56] The produced CO signal was detected when the temperature was raised to 450 °C (Figure S17), which confirms that *CO species are more easily desorbed and produce gaseous CO at high temperatures.[57,58] The absence of the gaseous CO signal at 250 °C is because the gaseous CO signal is too weak and difficult to detect in a highly diluted atmosphere and has low catalytic activity. Furthermore, except for the *CO pathway, other reaction routes of RWGS were observed on In_2O_3 NPs as well. For the pristine sample, only b-CO_3^{2-} and m-CO_3^{2-} were found at 250 °C (Figure 4e), which indicates that the carbonate route is another reaction mechanism leading to CO synthesis.[16,47]

In sharp contrast, HCO_3^-,[59,60] b-CO_3^{2-},[16,61] m-CO_3^{2-},[16,61] and formate (HCOO*)[16,58,61] were observed over the Vö-rich vacuum calcined sample at 250 °C (Figure 4e). The HCOO* is typically formed by further hydrogenation of carbonate, and the presence of HCOO* in the vacuum calcined sample indicates that stronger CO_2 adsorption strength on its surface makes more stable carbonate and enables further hydrogenation.[49] Furthermore, the same species, including HCOO*,[16,58,61] b-CO_3^{2-},[16,61] and m-CO_3^{2-},[16,61] were found in the spectra at 450 °C of both samples (Figure 4f). Such phenomena indicate that similar reaction pathways occur for both samples at 450 °C, consistent with similar E_a results. Therefore, the formation of surface Vö increases the adsorption capacity of CO_2, thereby improving the catalytic activity. The stronger carbonate adsorption strength caused by lattice expansion and the existence of multidentate carbonate on the Vö-rich surface stabilizes the carbonate species to further hydrogenate to form HCOO*. The schematic diagram shown in Figure 4g presents how the formation of Vö and lattice expansion alter the reaction pathways of the RWGS reaction. It also summarizes the relationship between temperature and the degree of surface lattice expansion, as well as the correlation between lattice expansion, the CO rate, and the E_a of the RWGS reaction. It is well known that the change of E_a indicates the alteration of reaction mechanism or interactions of surface-active sites on reactants/intermediates/products.[62] In our case, the E_a decreased from 132.90 to 87 kJ/mol after the temperature exceeded 350 °C. Though there is a significant increase of oxygen vacancies in the In_2O_3 when the temperature ramps from lower ones to exceed 350 °C, increasing the number instead of the type of active sites cannot explain the change in E_a. Further investigation revealed that this was due to the irreversible lattice expansion that regulated the electronic states of the surface sites with regard to the promoted CO_2 adsorption. Stronger CO_2 adsorption strength

https://doi.org/10.1021/jacs.4c12985
J. Am. Chem. Soc. XXXX, XXX, XXX−XXX

was beneficial to stabilize the carbonate for further hydrogenation to form a new formate pathway.

The structure of postreaction In_2O_3 was analyzed. Figure S19a shows that the (222) lattice plane expansion can still be observed as the surface *d*-spacing of 3.13 Å, expanded by 7.2%, and the subsurface *d*-spacing of 3.06 Å expanded by 4.8%. In addition, the results from the ELNES of the O-*K* edge confirm the presence of the Vö at both surface and center regions (Figure S19b). The intensity ratios between Peak A and Peak B are 0.885 ± 0.01 for the surface and 0.921 ± 0.006 for the center regions, respectively. These features indicate the presence of Vö after the RWGS reaction. Furthermore, the XPS 1s spectrum of the used In_2O_3 NPs presents a higher [Vö] compared to that of a fresh sample (Figure S20).

3. CONCLUSIONS

The question of how lattice thermal expansion is manifest in thermochemical heterogeneous catalysis has been addressed in the work described herein using a combination of *in situ* electron microscopy, diffraction, spectroscopy solid-state characterization techniques, and DFT. Using nanocrystalline indium oxide as a case in point, an irreversible thermally induced surface lattice expansion is traced to the formation of surface oxygen vacancies, which collectively enhances the catalytic performance for the exemplary reverse water gas shift reaction, an observation that receives support from DFT simulations. Quantitative insights into the effect of temperature on the structure, property, and chemical reactivity relations are pivotal for deconvoluting the contributing effects of thermal energy in heterogeneous catalysis.

4. EXPERIMENTAL SECTION

4.1. Synthesis of $In(OH)_3$ Nanocrystals. The synthesis of $In(OH)_3$ nanocrystals referred to in this work has been reported previously and involved the following synthesis steps: indium(III) chloride (3.6 g, 16.2 mmol, 99.99%) was dissolved in a 3:1 solution (72 mL) of anhydrous ethanol (Commercial Alcohols) and deionized water.[16] In a separate beaker, a 3:1 mixture of ethanol and ammonium hydroxide was prepared by combining an aqueous ammonium hydroxide (18 mL, 25−28%) with anhydrous ethanol (54 mL). The solutions were rapidly combined, resulting in the immediate formation of a white precipitate. The resulting suspension was then immediately immersed in a preheated oil bath at 80 °C and stirred for 30 min. The suspension was then removed from the oil bath and cooled to room temperature. The precipitate was separated via centrifugation and washed five times with deionized water. The precipitate was sonicated between washings to ensure adequate removal of any trapped impurities and then dried overnight at 60 °C in a vacuum oven.

4.2. Synthesis of Pristine In_2O_3 and Heat-Treated Samples. The pristine In_2O_3 nanocrystal (pristine) was obtained via the thermal treatment of the $In(OH)_3$ nanocrystal in air at 700 °C for 5 h in a muffle furnace with a ramp rate of 5 °C per minute. The vacuum calcined sample was obtained via thermal treatment of pristine In_2O_3 at 450 °C for 1 h in a tubular furnace with a ramp rate of 5 °C per minute under a vacuum pressure of ∼2.5 × 10^{-2} Pa (Rotary Vane Vacuum Pump, R-8SN, WIGGENS).

4.3. *In Situ* TEM Imaging and EELS Analysis. The real-time *in situ* (S)TEM observations were conducted by using a single-tilt Hitachi Blaze heating holder in a Hitachi HF-3300 environmental TEM/STEM operating at an accelerating voltage of 300 kV. The HF-3300 is equipped with a cold field-emission gun. The STEM images were acquired using a convergence angle of 18 mrad in high-resolution mode. EELS results were recorded using an EELS collection angle of 149 mrad. Energy dispersions of 0.25 eV/channel were used to acquire In-*M* and O-*K* edges, respectively. The energy resolutions in EELS, as measured by the full width at half-maximum of the zero-loss peak, was 1.0−1.3 eV. The energy scale for the EEL spectra of In_2O_3 NPs was calibrated by setting the edge maximum point of the O-*K* edge to 532 eV. The Gaussian function was used to deconvolute O-*K* peaks, whose results are shown in Figure S21.

During the *in situ* heating process, the temperature was increased in steps from RT (24 °C) to each targeted temperature at a heating rate of 1 °C/s. The holding time at each temperature was 20 min while the beam valve was closed to avoid electron beam irradiation.

4.4. DFT Calculation. All spin-polarized calculations were performed using the CASTEP package with the following convergence criteria: energy 5.0 × 10^{-5} eV/atom, max. force 0.1 eV/Å, max. stress 0.2 GPa, max. displacement 0.005 Å, and SCF tolerance 1.0 × 10^{-5} eV/atom.[63] To understand the experimentally observed lattice expansion, the (111) surface consisted of 1 × 1, four In−O layers, and a vacuum slab of 15 Å. The oxygen vacancy ([Vö])-laden surface was crafted by abstracting O atoms at different sites. The GGA-RPBE functional was used for the exchange−correlation potential, and the plane-wave pseudopotential approach and ultrasoft pseudopotentials were employed for all of the atoms with a kinetic energy cutoff of 260 eV. All models were first fully relaxed via geometry optimization and then applied for the energy calculation. The displacement of In, specifically along the [111] direction, can be obtained by the change in atomic position between [Vö]-laden model and the pristine model. For example, assuming (x_1, y_1, z_1) and (x_2, y_2, z_2) represent the Cartesian atomic position of pristine and [Vö]-laden indium oxide, then the [Vö]-induced displacement of In can be computed by (z_2 − z_1) since the [111] direction is along the *z* direction in our computation.

The [Vö] formation energies are defined as

$$E_{\text{form}}[\text{Vö}] = E_{[\text{Vö}]\text{-surf}} + 1/2\text{EO}_2 - E_{\text{surf}}$$

where [Vö]-surf represents the [Vö]-laden model and surf represents the pristine model of indium oxide.

4.5. Catalytic Activity Measurements. Gas-phase flow reactor measurements were carried out in a custom-built fixed-bed tubular reactor (8 mm outer diameter and 6 mm inner diameter). Within the reactor quartz tube, ∼20 mg of catalyst mixed with ∼150 mg of quartz sand was packed between two portions of quartz wool, which supported the packed catalyst bed in the center. External heating was provided by no-contact conduction via four heated ceramic rods surrounding the tubular reactor on two sides. A temperature controller managed the temperature by utilizing a thermocouple placed near the catalyst bed. During the reaction, H_2 and CO_2 flowed in a 1:1 ratio at a total volumetric flow rate of 12 mL min^{-1}. Product gases were analyzed using the flame ionization detector (FID) and thermal conductivity detector (TCD) installed in a gas chromatograph (Panna A91Plus, Changzhou Panna Instrument Co., Ltd.).

4.6. *In Situ* Diffuse Reflectance Infrared Fourier Transform Spectroscopy Characterization. *In situ* DRIFTS spectra were carried out in an *in situ* high-temperature reaction chamber (Praying Mantis HVC-DRM-5, Harrick Scientific) with a Fourier transform infrared spectrometer (Nicolet iS50, Thermo Fisher Scientific) and an MCT detector. First, the samples were pretreated at reaction temperature for 1 h in He at a 20 mL min^{-1} flow rate and then cooled to room temperature. Subsequently, a background spectrum was collected in He at the corresponding temperature before the catalyst was exposed to the analysis gas. The catalysts would be exposed to mixed gas (10% CO_2, 10% H_2, and 80% He) at a flow rate of 20 mL min^{-1}. During the testing, a list of spectra was collected by 64 scans at a resolution of 4 cm^{-1} in the range of 4000−1000 cm^{-1}.

For the CO_2 adsorption DRIFTS testing, the samples were pretreated at 250 °C for 1 h in He at a 20 mL min^{-1} flow rate and then cooled to room temperature. Subsequently, a background spectrum was collected in He at the corresponding temperature before the catalyst was exposed to the CO_2 mixed gas. The catalysts were exposed to mixed gas (10% CO_2 and 90% He) at a flow rate of 20 mL min^{-1}. During the testing, a list of spectra was collected by 64 scans at a resolution of 4 cm^{-1} in the range of 4000−1000 cm^{-1}.

https://doi.org/10.1021/jacs.4c12985
J. Am. Chem. Soc. XXXX, XXX, XXX−XXX

4.7. *In Situ* X-ray Diffraction Characterization. *In situ* XRD patterns were recorded using an X-ray diffractometer (SmartLab, Rigaku) with a heating chamber under a vacuum pressure of ~2×10^{-3} Pa (EDWARDS Rotary Vane Vacuum Pump, RV3). The diffractometer used Cu Kα radiation at 30 kV, and data were collected in the range of 2θ between 20° and 70°.

4.8. *In Situ*/*Ex Situ* X-ray Photoelectron Spectroscopy Characterization. XPS was performed using an X-ray photoelectron spectrometer (Supra Axis+, Shimadzu Kratos) in an ultrahigh vacuum chamber with a base pressure of 5×10^{-9} Torr (1×10^{-8} Torr for *in situ* XPS). The spectrometer used an Al Kα X-ray source operating at 15 kV and 15 mA. The samples were coated onto carbon tape, and all results were calibrated to a C of 1s 284.5 eV.

4.9. CO_2-Temperature-Programmed Desorption. CO_2-TPD curves were carried out on a chemisorption apparatus (Auto Chem II 2920, Micromeritics) with a temperature-ramp rate of 10 °C min^{-1} from 50−700 °C after pretreatment at 250 °C for 2 h in Ar.

■ ASSOCIATED CONTENT

Supporting Information

The Supporting Information is available free of charge at https://pubs.acs.org/doi/10.1021/jacs.4c12985.

Ex situ characterization results of pristine In_2O_3 NPs, additional results of *in situ* TEM, XPS, and DRIFTS, methods of HRTEM lattice measurement and EELS edge analysis, details of DFT calculations, evaluation of electron beam effect, additional analysis of catalytic performance, and analysis of after-reaction In_2O_3 nanoparticles (PDF)

■ AUTHOR INFORMATION

Corresponding Authors

Jane Y. Howe − *Department of Materials Science and Engineering, University of Toronto, Toronto, Ontario M5S 3E4, Canada; Department of Chemical Engineering and Applied Chemistry, University of Toronto, Toronto, Ontario M5S 3E5, Canada;* orcid.org/0000-0001-9319-3988; Email: jane.howe@utoronto.ca

Lu Wang − *School of Science and Engineering, The Chinese University of Hong Kong, Shenzhen, 518172 Shenzhen, Guangdong, P. R. China;* orcid.org/0000-0002-4165-4022; Email: lwang@cuhk.edu.cn

Geoffrey A. Ozin − *Solar Fuels Group, Department of Chemistry, University of Toronto, Toronto, Ontario M5S 3H6, Canada;* orcid.org/0000-0002-6315-0925; Email: g.ozin@utoronto.ca

Authors

Chenyue Qiu − *Department of Materials Science and Engineering, University of Toronto, Toronto, Ontario M5S 3E4, Canada;* orcid.org/0000-0002-3703-4058

Junchuan Sun − *School of Science and Engineering, The Chinese University of Hong Kong, Shenzhen, 518172 Shenzhen, Guangdong, P. R. China;* orcid.org/0009-0009-7663-1259

Mengsha Li − *Center for Microscopy and Analysis, Nanjing University of Aeronautics and Astronautics, Nanjing, Jiangsu 210016, P. R. China;* orcid.org/0000-0001-8437-0727

Chengliang Mao − *Solar Fuels Group, Department of Chemistry, University of Toronto, Toronto, Ontario M5S 3H6, Canada*

Rui Song − *Solar Fuels Group, Department of Chemistry, University of Toronto, Toronto, Ontario M5S 3H6, Canada*

Zeshu Zhang − *Ganjiang Innovation Academy, Chinese Academy of Sciences, Ganzhou 341000, P. R. China*

Doug D. Perovic − *Department of Materials Science and Engineering, University of Toronto, Toronto, Ontario M5S 3E4, Canada*

Complete contact information is available at: https://pubs.acs.org/10.1021/jacs.4c12985

Author Contributions

$^{\nabla}$C.Q., J.S., and M.L contributed equally to this work.

Notes

The authors declare no competing financial interest.

■ ACKNOWLEDGMENTS

The authors thank Dr. Zhentao Ma and Prof. Xusheng Zheng in the beamline BL10B in the National Synchrotron Radiation Laboratory (NSRL, Hefei Light Source) for the synchrotron radiation XPS characterization. J.S. and L.W. appreciate the support of the National Key R&D Program of China (Grant No. 2021YFF0502000). This work is funded by the Natural Sciences and Engineering Research Council of Canada (NSERC)'s Discovery Grants awarded to D.D.P. (RGPIN-2018-06492) and J.Y.H (RGPIN-2019-06444). All electron microscopy experiments were performed at the Open Centre for the Characterization of Advanced Materials (OCCAM), funded by the Canada Foundation for Innovation (CFI), and Center for Microscopy and Analysis at Nanjing University of Aeronautics and Astronautics for aberration-corrected TEM/STEM imaging. M.L. acknowledges the funding support from the Young Scientists Fund of the National Natural Science Foundation of China (Grant No. 52403297), the National Natural Science Foundation of Jiangsu Province (Grant No. BK20241426), and the Young Elite Scientists Sponsorship Program of Jiangsu Association for Science and Technology (Grant No. JSTJ-2024-010). C.M. acknowledges the financial support from the University of Toronto's Arts & Science Postdoctoral Fellowship and the National Supercomputer Centre in Shenzhen (China) for providing high-performance computation. J.S. and L.W. appreciate the support of the National Natural Science Foundation of China (Grant No. 52102311), the Program for Guangdong Introducing Innovative and Entrepreneurial Teams (Grants No. 2019ZT08L101), the Special Fund for the Sci-tech Innovation Strategy of Guangdong Province (Grants No. 21062905860472), the Shenzhen Natural Science Foundation (Grant Nos. GXWD20201231105722002-20200824163747001), the Shenzhen Key Laboratory of Eco-materials and Renewable Energy (Grant No. ZDSYS20200922160400001), and the University Development Fund (Grant No. UDF01001721). G.A.O. acknowledges the financial support of the Ontario Ministry of Research and Innovation (MRI), the Ministry of Economic Development, Employment and Infrastructure (MEDI), the Ministry of the Environment and Climate Change's (MOECC) Best in Science (BIS) Award, Ontario Centre of Excellence Solutions 2030 Challenge Fund, Ministry of Research Innovation and Science (MRIS), Low Carbon Innovation Fund (LCIF), Imperial Oil, the University of Toronto's Connaught Innovation Fund (CIF), Connaught Global Challenge (CGC) Fund, and the Natural Sciences and Engineering Research Council of Canada (NSERC). Thanks to Stas Dogel

https://doi.org/10.1021/jacs.4c12985
J. Am. Chem. Soc. XXXX, XXX, XXX−XXX

from Hitachi Canada and Norcada Inc. for their technical support.

REFERENCES

(1) Callister, W. D., Jr; Rethwisch, D. G. *Materials Science and Engineering - An Introduction*, 10th ed.; Wiley, 2018.
(2) Timoshenko, J.; Ahmadi, M.; Cuenya, B. R. Is There a Negative Thermal Expansion in Supported Metal Nanoparticles? An in Situ X-Ray Absorption Study Coupled with Neural Network Analysis. *J. Phys. Chem. C* **2019**, *123* (33), 20594−20604.
(3) Pishkenari, H. N.; Mohagheghian, E.; Rasouli, A. Molecular Dynamics Study of the Thermal Expansion Coefficient of Silicon. *Phys. Lett. A* **2016**, *380* (48), 4039−4043.
(4) Xiaoding, X.; Moulijn, Ja. Mitigation of CO2 by Chemical Conversion: Plausible Chemical Reactions and Promising Products. *Energy Fuels* **1996**, *10* (2), 305−325.
(5) Porosoff, M. D.; Yan, B.; Chen, J. G. Catalytic Reduction of CO2 by H2 for Synthesis of CO, Methanol and Hydrocarbons: Challenges and Opportunities. *Energy Environ. Sci.* **2016**, *9* (1), 62−73.
(6) Artz, J.; Müller, T. E.; Thenert, K.; Kleinekorte, J.; Meys, R.; Sternberg, A.; Bardow, A.; Leitner, W. Sustainable Conversion of Carbon Dioxide: An Integrated Review of Catalysis and Life Cycle Assessment. *Chem. Rev.* **2018**, *118* (2), 434−504.
(7) Ebikade, E. O.; Sadula, S.; Gupta, Y.; Vlachos, D. G. A Review of Thermal and Thermocatalytic Valorization of Food Waste. *Green Chem.* **2021**, *23* (8), 2806−2833.
(8) Zhang, W.; Ma, D.; Pérez-Ramírez, J.; Chen, Z. Recent Progress in Materials Exploration for Thermocatalytic, Photocatalytic, and Integrated Photothermocatalytic CO2 -to-Fuel Conversion. *Adv. Energy Sustainability Res.* **2022**, *3* (2), No. 2100169.
(9) Xu, L.; Yao, Q.; Deng, J.; Han, Z.; Zhang, Y.; Fu, Y.; Huber, G. W.; Guo, Q. Renewable N-Heterocycles Production by Thermocatalytic Conversion and Ammonization of Biomass over ZSM-5. *ACS Sustainable Chem. Eng.* **2015**, *3* (11), 2890−2899.
(10) Taylor, H. S. Mechanism of Activation at Catalytic Surfaces. *Proc. R. Soc. London, Ser. A* **1926**, *28* (1924), 77−86.
(11) Ghoussoub, M.; Xia, M.; Duchesne, P. N.; Segal, D.; Ozin, G. Principles of Photothermal Gas-Phase Heterogeneous CO2 Catalysis. *Energy Environ. Sci.* **2019**, *12* (4), 1122−1142.
(12) Zheng, H.; Meng, Y. S.; Zhu, Y. Frontiers of in Situ Electron Microscopy. *MRS Bull.* **2015**, *40* (1), 12−18.
(13) Zhang, X.; Han, S.; Zhu, B.; Zhang, G.; Li, X.; Gao, Y.; Wu, Z.; Yang, B.; Liu, Y.; Baaziz, W.; Ersen, O.; Gu, M.; Miller, J. T.; Liu, W. Reversible Loss of Core−Shell Structure for Ni−Au Bimetallic Nanoparticles during CO2 Hydrogenation. *Nat. Catal.* **2020**, *3* (4), 411−417.
(14) Frey, H.; Beck, A.; Huang, X.; van Bokhoven, J. A.; Willinger, M. G. Dynamic Interplay between Metal Nanoparticles and Oxide Support under Redox Conditions. *Science* **2022**, *987*, 982−987, DOI: 10.1126/science.abm3371.
(15) Hansen, P. L.; Wagner, J. B.; Helveg, S.; Rostrup-Nielsen, J. R.; Clausen, B. S.; Topsøe, H. Atom-Resolved Imaging of Dynamic Shape Changes in Supported Copper Nanocrystals. *Science* **2002**, *295* (5562), 2053−2055.
(16) Wang, L.; Dong, Y.; Yan, T.; Hu, Z.; Jelle, A. A.; Meira, D. M.; Duchesne, P. N.; Loh, J. Y. Y.; Qiu, C.; Storey, E. E.; Xu, Y.; Sun, W.; Ghoussoub, M.; Kherani, N. P.; Helmy, A. S.; Ozin, G. A. Black Indium Oxide a Photothermal CO2 Hydrogenation Catalyst. *Nat. Commun.* **2020**, *11* (1), No. 2432.
(17) Weiher, R. L.; Ley, R. P. Thermal Expansion of Indium Oxide. *J. Appl. Phys.* **1963**, *34* (6), 1833−1834.
(18) Frati, F.; Hunault, M. O. J. Y.; De Groot, F. M. F. Oxygen K-Edge X-Ray Absorption Spectra. *Chem. Rev.* **2020**, *120* (9), 4056−4110.
(19) Lei, F.; Sun, Y.; Liu, K.; Gao, S.; Liang, L.; Pan, B.; Xie, Y. Oxygen Vacancies Confined in Ultrathin Indium Oxide Porous Sheets for Promoted Visible-Light Water Splitting. *J. Am. Chem. Soc.* **2014**, *136* (19), 6826−6829.
(20) Gatan Ametek EELS Atlas. https://eels.info/atlas/indium. (accessed January 08, 2024).
(21) Kim, H. S.; Kim, Y. J.; Son, Y. R.; Pham, V. N.; Kim, K. j.; Kim, C. W.; Youn, Y. S.; Kwon, O. H.; Lee, H. Verifying the Relationships of Defect Site and Enhanced Photocatalytic Properties of Modified ZrO2 Nanoparticles Evaluated by In-Situ Spectroscopy and STEM-EELS. *Sci. Rep.* **2022**, *12* (1), No. 11295.
(22) Liu, C.; Mensching, B.; Volz, K.; Rauschenbach, B. Lattice Expansion of Ca and Ar Ion Implanted GaN. *Appl. Phys. Lett.* **1997**, *71* (16), 2313−2315.
(23) Richter, B.; Kuhlenbeck, H.; Freund, H. J.; Bagus, P. S. Cluster Core-Level Binding-Energy Shifts: The Role of Lattice Strain. *Phys. Rev. Lett.* **2004**, *93* (2), No. 026805, DOI: 10.1103/PhysRevLett.93.026805.
(24) Xu, H. Y.; Huang, Y. H.; Liu, S.; Xu, K. W.; Ma, F.; Chu, P. K. Effects of Annealing Ambient on Oxygen Vacancies and Phase Transition Temperature of VO2 Thin Films. *RSC Adv.* **2016**, *6* (83), 79383−79388.
(25) Zhuang, G.; Chen, Y.; Zhuang, Z.; Yu, Y.; Yu, J. Oxygen Vacancies in Metal Oxides: Recent Progress towards Advanced Catalyst Design. *Sci. China Mater.* **2020**, *63* (11), 2089−2118.
(26) Pathak, A.; Pandey, S. K.; Behera, J. K. Optical Band-Gap Evolution and Local Structural Change in Ge2Sb2Te5phase Change Material. *J. Phys.: Conf. Ser.* **2023**, *2426* (1), No. 012045.
(27) Böer, K. W.; Pohl, U. W. *Semiconductor Physics*; Springer, 2018.
(28) Gao, L.; Tang, C.; Liu, J.; He, L.; Wang, H.; Ke, Z.; Li, W.; Jiang, C.; He, D.; Cheng, L.; Xiao, X. Oxygen Vacancy-Induced Electron Density Tuning of Fe3O4 for Enhanced Oxygen Evolution Catalysis. *Energy Environ. Mater.* **2021**, *4* (3), 392−398.
(29) Dupin, J. C.; Gonbeau, D.; Vinatier, P.; Levasseur, A. Systematic XPS Studies of Metal Oxides, Hydroxides and Peroxides. *Phys. Chem. Chem. Phys.* **2000**, *2* (6), 1319−1324.
(30) Zhao, Z.; Wang, P.; Song, C.; Zhang, T.; Zhan, S.; Li, Y. Enhanced Interfacial Electron Transfer by Asymmetric Cu-Ov-In Sites on In2O3 for Efficient Peroxymonosulfate Activation. *Angew. Chem., Int. Ed.* **2023**, *62* (11), No. e20221640.
(31) Zhang, Z.; Mao, C.; Meira, D. M.; Duchesne, P. N.; Tountas, A. A.; Li, Z.; Qiu, C.; Tang, S.; Song, R.; Ding, X.; Sun, J.; Yu, J.; Howe, J. Y.; Tu, W.; Wang, L.; Ozin, G. A. New Black Indium Oxide–Tandem Photothermal CO2-H2Methanol Selective Catalyst. *Nat. Commun.* **2022**, *13* (1), No. 1512.
(32) Wei, Z.; Wang, W.; Li, W.; Bai, X.; Zhao, J.; Tse, E. C. M.; Phillips, D. L.; Zhu, Y. Steering Electron−Hole Migration Pathways Using Oxygen Vacancies in Tungsten Oxides to Enhance Their Photocatalytic Oxygen Evolution Performance. *Angew. Chem., Int. Ed.* **2021**, *60* (15), 8236−8242.
(33) Xiong, H.; Dong, Y.; Hu, C.; Chen, Y.; Liu, H.; Long, R.; Kong, T.; Xiong, Y. Highly Efficient and Selective Light-Driven Dry Reforming of Methane by a Carbon Exchange Mechanism. *J. Am. Chem. Soc.* **2024**, *146* (13), 9465−9475.
(34) Zhang, B.; Zhang, S.; Liu, B. Effect of oxygen vacancies on ceria catalyst for selective catalytic reduction of NO with NH3. *Appl. Surf. Sci.* **2020**, *529*, No. 147068.
(35) Wu, X.; Yu, X.; He, X.; Jing, G. Insight into Low-Temperature Catalytic NO Reduction with NH3 on Ce-Doped Manganese Oxide Octahedral Molecular Sieves. *J. Phys. Chem. C* **2019**, *123* (17), 10981−10990.
(36) Wang, B.; Wang, X.; Lu, L.; Zhou, C.; Xin, Z.; Wang, J.; Ke, X. K.; Sheng, G.; Yan, S.; Zou, Z. Oxygen-Vacancy-Activated CO2 Splitting over Amorphous Oxide Semiconductor Photocatalyst. *ACS Catal.* **2018**, *8* (1), 516−525.
(37) Schaub, R.; Wahlström, E.; Rønnau, A.; Lægsgaard, E.; Stensgaard, I.; Besenbacher, F. Oxygen-Mediated Diffusion of Oxygen Vacancies on the TiO2(110) Surface. *Science* **2003**, *299* (5605), 377−379.
(38) Scheiber, P.; Fidler, M.; Dulub, O.; Schmid, M.; Diebold, U.; Hou, W.; Aschauer, U.; Selloni, A. (Sub)Surface Mobility of Oxygen Vacancies at the TiO2 Anatase (101) Surface. *Phys. Rev. Lett.* **2012**, *109* (13), No. 136103.

(39) Cao, A.; Wang, Z.; Li, H.; Nørskov, J. K. Relations between Surface Oxygen Vacancies and Activity of Methanol Formation from CO2 Hydrogenation over In2O3 Surfaces. *ACS Catal.* **2021**, *11* (3), 1780−1786.
(40) Truhlar, D. G.; Kohen, A. Convex Arrhenius Plots and Their Interpretation. *Proc. Natl. Acad. Sci. U.S.A.* **2001**, *98* (3), 848−851.
(41) Liang, S.; An, Q.; Wang, S.; Chen, Z.; Huang, L.; Zhao, L. Sub-3 Nm CoO Nanoparticles with Oxygen Vacancy-Dependent Catalytic Activity for the Oxygen Reduction Reaction. *ACS Appl. Nano Mater.* **2022**, *5* (6), 8214−8223.
(42) Ye, J.; Liu, C.; Mei, D.; Ge, Q. Active Oxygen Vacancy Site for Methanol Synthesis from CO2 Hydrogenation on In2O3(110): A DFT Study. *ACS Catal.* **2013**, *3* (6), 1296−1306.
(43) Yu, K.; Lou, L. L.; Liu, S.; Zhou, W. Asymmetric Oxygen Vacancies: The Intrinsic Redox Active Sites in Metal Oxide Catalysts. *Adv. Sci.* **2020**, *7* (2), No. 1901970.
(44) Mino, L.; Spoto, G.; Ferrari, A. M. CO2 Capture by TiO2 Anatase Surfaces: A Combined DFT and FTIR Study. *J. Phys. Chem. C* **2014**, *118* (43), 25016−25026.
(45) Lorber, K.; Zavašnik, J.; Arčon, I.; Huš, M.; Teržan, J.; Likozar, B.; Djinović, P. CO2 Activation over Nanoshaped CeO2 Decorated with Nickel for Low-Temperature Methane Dry Reforming. *ACS Appl. Mater. Interfaces* **2022**, *14* (28), 31862−31878.
(46) Wang, L.; Guan, E.; Wang, Y.; Wang, L.; Gong, Z.; Cui, Y.; Meng, X.; Gates, B. C.; Xiao, F. S. Silica Accelerates the Selective Hydrogenation of CO2 to Methanol on Cobalt Catalysts. *Nat. Commun.* **2020**, *11* (1), No. 1033.
(47) Busca, G.; Lorenzelli, V. Infrared Spectroscopic Identification of Species Arising From Reactive Adsorption of Carbon Oxides on Metal Oxide Surfaces. *Mater. Chem.* **1982**, *7* (1), 89−126.
(48) Collins, S. E.; Baltanás, M. A.; Bonivardi, A. L. Infrared Spectroscopic Study of the Carbon Dioxide Adsorption on the Surface of Ga2O3 Polymorphs. *J. Phys. Chem. B* **2006**, *110* (11), 5498−5507.
(49) Du, P.; Deng, G.; Li, Z.; Sun, J.; Wang, L.; Yang, Y.; Wang, J.; Li, Y.; Xu, X.; Zhang, Y.; Liu, W.; Liu, G.; Zou, Z.; Li, Z. Effective CO2 Activation of Enriched Oxygen Vacancies for Photothermal CO2Methanation. *J. Mater. Sci. Technol.* **2024**, *189*, 203−210.
(50) Baltrusaitis, J.; Jensen, J. H.; Grassian, V. H. FTIR Spectroscopy Combined with Isotope Labeling and Quantum Chemical Calculations to Investigate Adsorbed Bicarbonate Formation Following Reaction of Carbon Dioxide with Surface Hydroxyl Groups on Fe2O3 and Al2O3. *J. Phys. Chem. B* **2006**, *110* (24), 12005−12016.
(51) Taifan, W.; Boily, J. F.; Baltrusaitis, J. Surface Chemistry of Carbon Dioxide Revisited. *Surf. Sci. Rep.* **2016**, *71* (4), 595−671.
(52) Wei, W.; Wei, Z.; Li, R.; Li, Z.; Shi, R.; Ouyang, S.; Qi, Y.; Philips, D. L.; Yuan, H. Subsurface Oxygen Defects Electronically Interacting with Active Sites on In2O3 for Enhanced Photothermocatalytic CO2 Reduction. *Nat. Commun.* **2022**, *13* (1), No. 3199.
(53) Liu, H. X.; Li, J. Y.; Qin, X.; Ma, C.; Wang, W. W.; Xu, K.; Yan, H.; Xiao, D.; Jia, C. J.; Fu, Q.; Ma, D. Ptn−Ov Synergistic Sites on MoOx/γ-Mo2N Heterostructure for Low-Temperature Reverse Water−Gas Shift Reaction. *Nat. Commun.* **2022**, *13* (1), No. 5800.
(54) Yan, T.; Li, N.; Wang, L.; Ran, W.; Duchesne, P. N.; Wan, L.; Nguyen, N. T.; Wang, L.; Xia, M.; Ozin, G. A. Bismuth Atom Tailoring of Indium Oxide Surface Frustrated Lewis Pairs Boosts Heterogeneous CO2 Photocatalytic Hydrogenation. *Nat. Commun.* **2020**, *11* (1), No. 6095.
(55) Hu, J.; Yu, L.; Deng, J.; Wang, Y.; Cheng, K.; Ma, C.; Zhang, Q.; Wen, W.; Yu, S.; Pan, Y.; Yang, J.; Ma, H.; Qi, F.; Wang, Y.; Zheng, Y.; Chen, M.; Huang, R.; Zhang, S.; Zhao, Z.; Mao, J.; Meng, X.; Ji, Q.; Hou, G.; Han, X.; Bao, X.; Wang, Y.; Deng, D. Sulfur Vacancy-Rich MoS2 as a Catalyst for the Hydrogenation of CO2 to Methanol. *Nat. Catal.* **2021**, *4* (3), 242−250.
(56) Huynh, H. L.; Zhu, J.; Zhang, G.; Shen, Y.; Tucho, W. M.; Ding, Y.; Yu, Z. Promoting Effect of Fe on Supported Ni Catalysts in CO2Methanation by in Situ DRIFTS and DFT Study. *J. Catal.* **2020**, *392*, 266−277.
(57) Wang, X.; Shi, H.; Kwak, J. H.; Szanyi, J. Mechanism of CO2 Hydrogenation on Pd/Al2O3 Catalysts: Kinetics and Transient DRIFTS-MS Studies. *ACS Catal.* **2015**, *5* (11), 6337−6349.
(58) Bobadilla, L. F.; Santos, J. L.; Ivanova, S.; Odriozola, J. A.; Urakawa, A. Unravelling the Role of Oxygen Vacancies in the Mechanism of the Reverse Water-Gas Shift Reaction by Operando DRIFTS and Ultraviolet-Visible Spectroscopy. *ACS Catal.* **2018**, *8* (8), 7455−7467.
(59) Yu, X.; Ding, X.; Yao, Y.; Gao, W.; Wang, C.; Wu, C.; Wu, C.; Wang, B.; Wang, L.; Zou, Z. Layered High-Entropy Metallic Glasses for Photothermal CO2Methanation. *Adv. Mater.* **2024**, *36* (21), No. 2312942.
(60) Lu, Z.; Xu, Y.; Zhang, Z.; Sun, J.; Ding, X.; Sun, W.; Tu, W.; Zhou, Y.; Yao, Y.; Ozin, G. A.; Wang, L.; Zou, Z. Wettability Engineering of Solar Methanol Synthesis. *J. Am. Chem. Soc.* **2023**, *145* (48), 26052−26060.
(61) Yan, T.; Wang, L.; Liang, Y.; Makaremi, M.; Wood, T. E.; Dai, Y.; Huang, B.; Jelle, A. A.; Dong, Y.; Ozin, G. A. Polymorph Selection towards Photocatalytic Gaseous CO2 Hydrogenation. *Nat. Commun.* **2019**, *10* (1), No. 2521.
(62) Chang, F.; Guan, Y.; Chang, X.; Guo, J.; Wang, P.; Gao, W.; Wu, G.; Zheng, J.; Li, X.; Chen, P. Alkali and Alkaline Earth Hydrides-Driven N2 Activation and Transformation over Mn Nitride Catalyst. *J. Am. Chem. Soc.* **2018**, *140* (44), 14799−14806.
(63) Clark, S. J.; Segall, M. D.; Pickard, C. J.; Hasnip, P. J.; Probert, M. I. J.; Refson, K.; Payne, M. C. First Principles Methods Using CASTEP. *Z. Kristallogr. - Cryst. Mater.* **2005**, *220* (5−6), 567−570.

https://doi.org/10.1021/jacs.4c12985
J. Am. Chem. Soc. XXXX, XXX, XXX−XXX